A Fractional-Order Wireless Power Transfer System With Misalignment and Detuning Tolerance

Chao Rong and Bo Zhang, *Senior Member, IEEE*

***Abstract*—For wireless power transfer (WPT) systems, parameter fluctuations and misalignment of coils will lead to frequency detuning, which will, in turn, affect system performance and output accuracy. In general, the conventional frequency-tuning strategies rely on adjustable capacitors or inductors, which increase the control complexity or require additional modules. Therefore, this article proposes a fractional-order WPT system with adjustable fractional order. The proposed system with misalignment and detuning tolerance can provide a constant current (CC) or constant voltage (CV) output. First, based on the coupled mode theory, the frequency and output characteristics are analyzed. Then, a frequency-tuning strategy based on the fractance element is proposed. Operation modes and equivalent impedance of the fractance element are analyzed. On this basis, control strategies of CC and CV are designed for the transmitter and receiver, respectively, Finally, an 864-W prototype is set up to validate the proposed frequency-tuning strategy and control strategy. The proposed system has robustness to misalignment and parameter fluctuations, which can improve efficiency and output accuracy.**

***Index Terms*—Constant current (CC)/voltage charging, fractance, frequency tuning, wireless power transfer (WPT).**

I. Introduction

WIRELESS power transfer (WPT) is a new type of power transmission and is changing the scheme of power supply in various fields [1]. Due to its unique safety, convenience, and reliability, WPT is expected to become the ideal solution for reliable energy supply in the fields of automatic guided vehicles (AGV), electric vehicles, and implanted medical equipment. With the development of AGV, the Li-ion battery is the key component for storing and providing energy, and its safety and reliability are crucial to the entire system. The high-cost problem caused by installing many batteries can be effectively solved by WPT. Obviously, WPT will play an important role in various intelligent and unmanned applications. In addition, the charging process of Li-ion battery is a complex electrochemical response. Therefore, the charging solution should not only inhibit the polarization effect, but also control the temperature rise, thereby improving the charging efficiency and service life of the battery. At present, charging methods for batteries mainly have continuous, intermittent, digital, and pulse charging methods. Among them, the continuous charging method in stages such as constant current (CC) and constant voltage (CV) is widely used [2].

In order to cope with different operating conditions, the control target of WPT systems mainly includes the adjustable output current or voltage, the detuning tolerance, and the misalignment tolerance. To achieve these control goals, the corresponding amount of control variable freedom is generally required. In terms of adjustable output current or voltage, the main solutions include the design of passive compensation topology, additional dc–dc converters, and controlled inverters and rectifiers. The parameter design of compensation topology can effectively reduce the sensitivity of output power to misalignment [3]. It does not require special coil design and complex control strategies. However, the coupling range and output accuracy still need to be improved. The reconstruction of compensation topology not only has a large size, but also fluctuates during the switching process [4], [5]. The additional dc–dc converters, as an additional circuit link, can cause a substantial loss of efficiency and it is not conducive to reducing costs and size [6]. In addition, a reconfigurable rectifier can effectively improve the coupling range and system efficiency without complex design [7]. Based on reconfigurable rectifiers, adding a clamping circuit can build another two stable operating regions to effectively improve misalignment tolerance [8]. A secondary active rectifier control scheme in [9] achieves constant output by controlling the effective impedance of the secondary. Different from the conventional control strategy of semibridge active rectifiers, this method avoids the additional reactive power and effectively improves transfer efficiency. In order to improve misalignment tolerance, the design of coils is one of the solutions for improving misalignment tolerance. This solution aims to reduce the variation of mutual inductance so that stable output can be achieved without complex control [10], [11], [12]. However, the problems such as limited transfer range and low output accuracy still need to be overcome.

In terms of the frequency detuning caused by parameter fluctuations, the main solutions include changing the operating frequency and using a dynamic compensation network. Changing the operating frequency in real-time to track the resonance frequency cannot adjust the resonance frequency of the transmitter and the receiver separately. Meanwhile, the limited adjustment range of frequency also brings limitations to this

Manuscript received 30 March 2023; revised 3 July 2023 and 28 August 2023; accepted 19 September 2023. Date of publication 26 September 2023; date of current version 23 October 2023. This work was supported in part by the Key Program of National Natural Science Foundation of China under Grant 52130705 and in part by the Key Program of National Natural Science Foundation of China under Grant 51437005. Recommended for publication by Associate Editor P. D. Mitcheson. *(Corresponding author: Bo Zhang.)*

The authors are with the School of Electric Power, South China University of Technology, Guangzhou 510640, China (e-mail: eprongchao@mail.scut.edu.cn; epbzhang@scut.edu.cn).

Color versions of one or more figures in this article are available at https://doi.org/10.1109/TPEL.2023.3319366.

Digital Object Identifier 10.1109/TPEL.2023.3319366

solution. The dynamic compensation network aims at changing values of capacitance or inductance in real-time, which can be divided into three categories: inductance or capacitor matrix [13], switch-controlled capacitor (SCC) [14], [15], [16], and variable inductor [17], [18]. The first category is generally with the help of the combination of inductance or capacitance to achieve impedance matching. Obviously, it is discontinuous to change the value of the passive component through the matrix switch, which will undoubtedly affect the output accuracy and dynamic process of the frequency tuning. In order to improve the speed of response, the methods of SCC and variable inductors are proposed. In [14], a double-side frequency tuning control with independent and adaptive compensation characteristics is proposed. Benefiting from the characteristics of continuous and rapid adjustment of SCC, the system has robustness to parameter fluctuations and has higher transfer efficiency and voltage gain. This system inevitably employs more capacitors and switches to construct switched capacitors and has power limitations. The third category is variable inductors. The principle of variable inductors is to change the magnetic permeability of the magnetic core by adjusting dc of the auxiliary winding, thereby controlling the inductance of the main winding. Although this method improves the adjustment range of the load, it inevitably increases the eddy-current loss of the variable inductor. In addition, redundant auxiliary coils and communication modules are often required to achieve double-side frequency tuning [16]. In summary, the dynamic compensation network can solve the problem of frequency detuning caused by parameter fluctuations, which has a fast response speed and a wide adjustment range. However, it also faces some problems, such as power limitation, high cost, and complex control.

In practical applications, the load and transfer distance vary over a wide range and frequency detuning is also inevitable. It can be found that the strategy of adjusting the operating frequency or dynamic compensation network cannot completely solve the above problems. Broadening the attention point to the fractional order, fractance elements have been successfully applied in many fields [19], [20]. By combining fractional calculus with WPT, a fractional-order WPT (FOWPT) system has been proposed. Benefiting from the frequency characteristics of active fractional-order capacitors, real-time parameter identification of mutual inductance and load can be achieved [21]. However, the accuracy of parameter identification depends heavily on self-inductance, capacitance, and sampling accuracy. For coils with ferrite, the self-inductance will vary with misalignment. Parameter fluctuations will put forward higher requirements for WPT systems. Fortunately, fractional order elements can not only flexibly adjust the output power and frequency, but also change the reactance component by adjusting the fractional order. Therefore, FOWPT has great potential to solve the problem of frequency detuning and achieving constant output.

This article will focus on the misalignment and frequency detuning in wireless charging systems of AGV. To overcome the above problems and achieve stable output, a FOWPT system is proposed and has the following features.

1) A FOWPT system based on the fractance element is proposed, and the coupled model of the detuned system is established. Compared to the circuit model, the coupled model reduces the order of the equation, making it possible to solve the characteristic frequencies. According to the operation modes of the fractance element, the soft switching is designed.
2) Based on the coupled model and an improved perturbation and observation (P&O) algorithm, a frequency-tuning strategy is proposed. Compared to other strategies, this strategy relies on the frequency characteristics of the system, which does not require wireless communication and complex structures.
3) CC and CV control strategies of transmitter and receiver are proposed respectively. The high-accuracy CC or CV output with misalignment tolerance and detuning tolerance is achieved, which relies on the coordination of the integer-order circuit on the transmitting side and the fractional-order circuit on the receiving side.

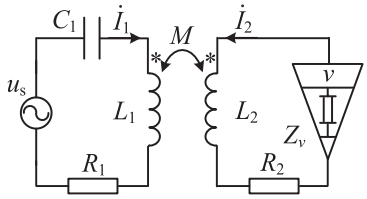

Fig. 1. Schematic diagram of the proposed FOWPT system.

Knowing these descriptions in mind, the rest of this article is organized as follows. In Section II, operation modes and equivalent parameters of the fractance element are analyzed, and a coupled model of the detuned system is established. Based on this model, a strategy of frequency tuning is proposed in Section III. Section IV designs CC or CV control strategies for transmitters and receivers. Subsequently, a prototype with misalignment tolerance and detuning tolerance is established in Section IV. Finally, Section V concludes this article.

II. System Structure and Detuning Characteristics

A. System Structure

Fig. 1 represents a schematic diagram of the proposed FOWPT system, which consists of an excitation source u_s, a compensation network, coils, and fractance element. The energy is wirelessly transmitted through mutual inductance M and ultimately supplied to the load through the fractance element.

The transmitter comprises a primary-side inductance L_1, a primary-side capacitance C_1, and an internal resistance R_1 that are connected in series. The receiver comprises a secondary-side inductance L_2, an internal resistance R_2, and fractance element Z_v that are connected in series. In addition, Z_v and v are the pseudo-impedance and fractional order of the fractance element, respectively. The characteristic equation of the fractance element can be expressed as

$$v(t) = Z_v \frac{d^v i(t)}{dt^v} \tag{1}$$

where the range of the fractional order v is $(-2, 2)$; $v(t)$ and $i(t)$ are the voltage and current of the fractance element, respectively.

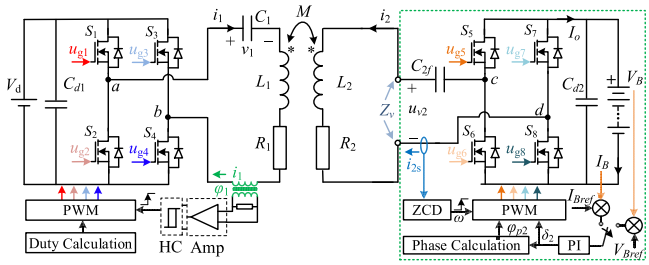

Fig. 2. Circuit diagram of the FOWPT system.

If v is a fraction, d^v/dt^v is termed as the fractional order derivative. The fractance element can be equivalent to resistance component $R_{Zv} = \omega^v Z_v \cos(v\pi/2)$ and reactance component $X_{Zv} = \omega^v Z_v \sin(v\pi/2)$. It is noted that the order v in the proposed system is designed to satisfy $-1 < v < 0$. And the fractance element can be equivalent to a capacitance and a positive resistance, which is beneficial for achieving frequency tuning and soft switching design.

According to the schematic diagram, the corresponding circuit diagram of the FOWPT system for frequency tuning and CC/CV charging is designed, as shown in Fig. 2. V_d is the dc voltage source. Four MOSFETs S_1–S_4 are controlled as a full-bridge inverter; the other MOSFETs S_5–S_8 and capacitor C_{2f} are controlled as a fractance element, which supplies energy to the battery. It is noted that R_B is the equivalent resistance of the battery. In the sampling circuit, the zero-crossing detection includes an amplifier (Amp) and a hysteresis comparator (HC).

The existing methods for constructing fractance elements mainly include arrays of RLC components, electrochemical methods, silicon process technology, and operational Amp circuits [22]. However, based on the above methods, the fractional order and output power cannot be flexibly adjusted according to the requirements of transfer distance and load. These approximate construction methods have significant limitations and cannot be applied in WPT systems. To construct a FOWPT system, this section will construct a fractance element with adjustable fractional order based on power electronic converters, as shown in the green dashed box in Fig. 2.

For WPT systems with high Q-values, high-order harmonics are hardly through it. Therefore, the fundamental wave analysis method is used to analyze the characteristics of the fractance element. According to the circuit theory, the excitation source $\dot{V}_{ab}$formed by the inverter can be expressed as

$$\dot{V}_{ab} = \frac{2\sqrt{2}V_d}{\pi} \sin\frac{\delta_1}{2} \angle\varphi_{p1} \tag{2}$$

where $\delta_1 = D_1\pi$ is the pulse width of the inverter; φ_{p1} is the phase difference between the current i_1 and the fundamental component v_{ab}. Similarly, voltage v_{cd} can be expressed as

$$\dot{V}_{cd} = \frac{2\sqrt{2}V_B}{\pi} \sin\frac{\delta_2}{2} \angle\varphi_{p2} \tag{3}$$

where $\delta_2 = D_2\pi$ is the pulse width of the fractance element; φ_{p2} is the phase difference between the current i_{2s} and the fundamental component v_{cd}. Adjusting δ_2 and φ_{p2} can flexibly adjust the output power and the natural resonant frequency of the receiver, thereby achieving efficient and stable WPT. In fact, the impedance and fractional order of Z_v are determined by the pulse width δ_2, phase φ_{p2}, and the load R_B.

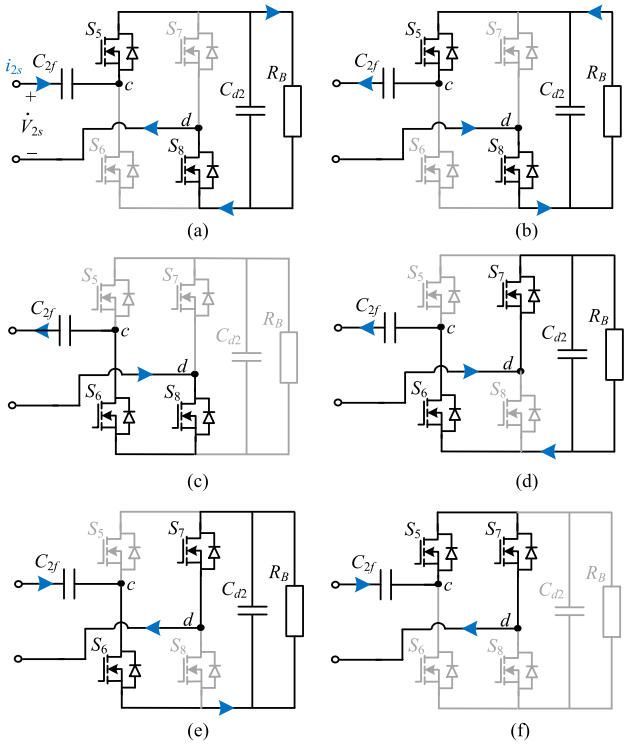

Fig. 3. Operation modes of the equivalent circuit of the fractance element.

In order to analyze the equivalent parameters and soft switching conditions of the fractance element, operation modes are shown in Fig. 3. u_{2s} and i_{2s} are the voltage and current of the fractance element, respectively. Generally, the phase of i_{2s} is controlled to be ahead of the phase of v_{cd} to facilitate the realization of soft switching. Based on the above design, The first half-cycle is described as follows.

Mode 1: Switches S_5 and S_8 are turned ON, and the system supplies power to C_{d2} and load R_B.

Mode 2: The current flows through switches S_5 and S_8 in the opposite direction, and the capacitor C_{d2} supplies energy to the system. After hard-switching off S_5 and soft-switching on S_6, mode 3 comes.

Mode 3: During this mode, v_{cd} is zero. The current flows through the antiparallel diodes of switches S_6 and S_8. The load R_B is powered by the capacitor C_{d2}. After hard-switching off S_8 and soft-switching on S_7, mode 4 comes.

Mode 4: The current flows through switches S_6 and S_7 in the opposite direction, and the system supplies power to capacitor C_{d2} and load $\mathrm{R_B}$.

Mode 5: Switches S_6 and S_7 are turned ON, and the capacitor C_{d2} supplies energy to the system. After hard-switching off S_6 and soft-switching on S_5, mode 6 comes.

Mode 6: During this mode, v_{cd} is zero. The current flows through S_7 and the antiparallel diodes of switches S_5. The load R_B is powered by the capacitor C_{d2}. And then S_7 is turned OFF with hard-switching and S_8 is turned ON with soft-switching.

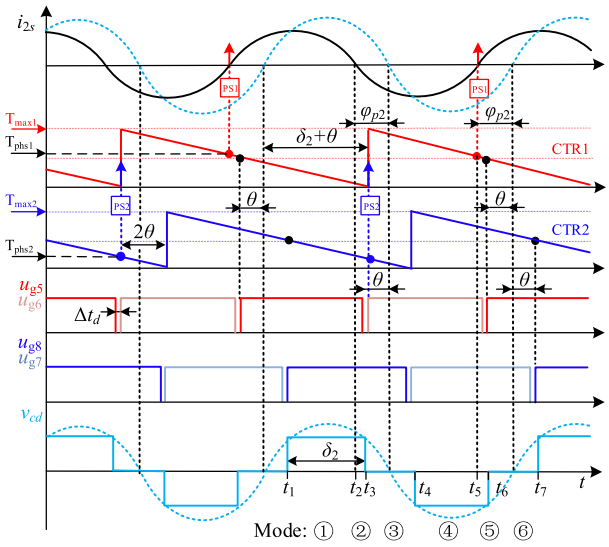

Fig. 4. Control signals and operating waveforms of the fractance element.

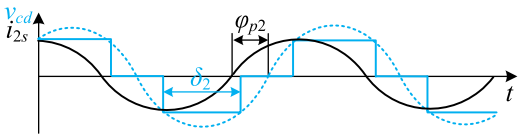

Fig. 5. Waveform diagram of voltage v_{cd} and current i_{2s}.

Fig. 4 depicts the control signals and operating waveforms of the fractance element, where the operation modes 1–6 in Fig. 3 are listed in detail. The current i_{2s} is ahead of the voltage v_{cd}; the pulse width δ_2 and phase θ can be expressed as $D_2\pi$ and $(1-D_2)\pi/2$, respectively. The counter CTR1 of the c-bridge arm lags the counter CTR2 of the d-bridge arm, and the lagging phase is 2θ. First, the high-frequency current i_{2s} in the receiver generates an in-phase square wave signal through a sampling circuit, a phase compensation network, and a HC. The digital controller obtains the phase and frequency of i_{2s} by capturing the rising edge PS1 of the square wave. Then, the counters CTR1 and CTR2 of the two PWM modules are in the down count mode. The drive signal $u_{g5\text{-}8}$ will flip the level at 0 and $0.5{*}\mathrm{T}_{\mathrm{max1,2}}$. In addition, two switches of the same bridge arm reserve a certain dead time to release the charge from the output capacitors of MOSFETs. Finally, through phase control, the voltage v_{cd} is generated. The lead phase φ_{p2} can be controlled by regulating the values of $\mathrm{T}_{\mathrm{phs1}}$ to adjust the resonant frequency of the receiver. By adjusting the synchronization phase $\mathrm{T}_{\mathrm{phs2}}$, the pulse width δ_2 of v_{cd} can be changed to adjust the output current or voltage. For the transmitter, when the corresponding φ_{p1} is controlled to 0, the output voltage v_{ab} of the inverter is in phase with the output current i_1, and the transmitter is in zero-phase mode.

Fig. 5 shows the waveform diagram of voltage v_{cd} and current i_{2s}, where the phase of i_{2s} is ahead of the phase of v_{cd}, and the lead phase is φ_{p2}. v_{cd} and φ_{p2} can be adjusted by the controller. Assuming that the current $i_{2s}=\sqrt{2}I_{2s}\sin\omega t$, it can be obtained that

$$V_2\angle\varphi_v=\frac{I_{2s}}{\omega C_{2f}}\angle(\pi/2)+Z_{cd}I_{2s}\angle\varphi_{cd}. \tag{4}$$

According to (3), the voltage $\dot{V}_{cd}$ can be expressed as

$$\dot{V}_{cd}=\frac{2\sqrt{2}}{\pi}R_BI_B\sin(\delta_2/2)\,e^{-j\varphi_{p2}}. \tag{5}$$

When the loss of switches is ignored, it can be obtained that the current I_B of the load R_B can be expressed as

$$\begin{aligned}I_B&=\frac{1}{\pi}\int_{\frac{\pi}{2}-\frac{\delta_2}{2}+\varphi_{p2}}^{\frac{\pi}{2}+\frac{\delta_2}{2}+\varphi_{p2}}\sqrt{2}I_{2s}\sin(\omega t)\,d(\omega t)\\&=\frac{2\sqrt{2}}{\pi}I_{2s}\cos\varphi_{p2}\sin(\delta_2/2).\end{aligned} \tag{6}$$

Thus, the equivalent impedances of ports c and d can be expressed as

$$\begin{aligned}Z_{cd}\angle\varphi_{cd}&=\frac{\dot{V}_{cd}}{\dot{I}_{2s}}=R_{cd}+jX_{cd}\\&=\frac{4}{\pi^2}R_B(1-\cos\delta_2)\left(\cos^2\varphi_{p2}-j\cos\varphi_{p2}\sin\varphi_{p2}\right).\end{aligned} \tag{7}$$

According to (4) and (7), the pseudo-impedance Z_v and fractional order v of the fractance element can be expressed as

$$\begin{cases}|Z_v|=\sqrt{R_{cd}^2+\left[X_{cd}-\frac{1}{\omega C_{2f}}\right]^2}\\ v=\frac{\pi}{2}\arctan\frac{X_{cd}-\frac{1}{\omega C_{2f}}}{R_{cd}}\end{cases}. \tag{8}$$

Then the corresponding equivalent resistance and reactance can be derived as

$$\begin{cases}R_v=\frac{4}{\pi^2}R_B(1-\cos\delta_2)\cos^2\varphi_{p2}\\ X_v=-\frac{1}{\omega C_{2f}}-\frac{4}{\pi^2}R_B(1-\cos\delta_2)\cos\varphi_{p2}\sin\varphi_{p2}\end{cases}. \tag{9}$$

It is worth noting that the designed fractance element is more general. Its pseudo-impedance and fractional order can be adjusted in real-time according to requirements of frequency detuning and output. Considering that the range of the phase φ_{p2} is $(0, \pi/2)$, the corresponding equivalent capacitance C_2 can be expressed as

$$C_2=\frac{\pi^2C_{2f}}{4\omega R_B(1-\cos\delta_2)\cos\varphi_{p2}\sin\varphi_{p2}C_{2f}+\pi^2}. \tag{10}$$

It can be found from (9) and (10) that the equivalent parameters of the fractance element are not only related to the control variables φ_{p2} and δ_2, but also to the load R_B and capacitance C_{2f}. Importantly, the accuracy of capacitance C_{2f} of fractance element is crucial. Therefore, multilayer ceramic capacitors with C0G dielectric are employed, which are connected in series and parallel to construct the capacitor C_{2f}. Fig. 6 draws the equivalent resistance and capacitance adjustment range of the fractance element when $R_B=50\ \Omega$. On the one hand, the equivalent resistance R_v increases with the increase of δ_2 and decreases with the increase of φ_{p2}. On the other hand, the equivalent capacitance C_2 decreases with the increase of δ_2; it decreases

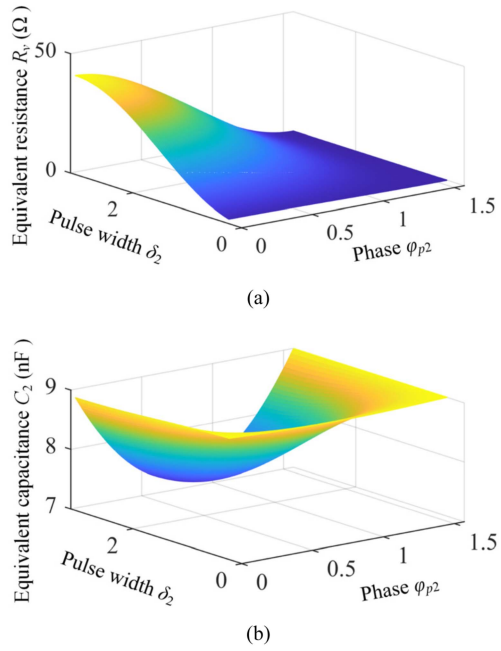

Fig. 6. Equivalent resistance and capacitance adjustment range of the fractance element. (a) Equivalent resistance R_v. (b) Equivalent capacitance C_2.

first and then increases as φ_{p2} increases. There is a minimum value when $\varphi_{p2} = \pi/4$. Meanwhile, the larger the capacitive reactance provided by the fractance element, the narrower the adjustment range of its equivalent resistance. The maximum equivalent resistance that can be transformed is within the range of $[4R_B/\pi^2, 8R_B/\pi^2]$. Therefore, when designing the output characteristics of the system, it is necessary to fully consider the impedance characteristics of the fractance element to meet the requirements of CC and CV.

B. System Model and Frequency Characteristic

In the proposed system, the transmitter is an integer-order circuit. In order to achieve frequency tuning of the system, the inverter is controlled to be in zero-phase mode, i.e., the output voltage v_{ab} of the inverter is in phase with the output current i_1. Considering (2), v_{ab} of the inverter in Fig. 2 can be expressed as

$$v_{ab} = \frac{4V_d}{\pi} \sin\frac{\delta_1}{2} \frac{i_1}{|i_1|} \tag{11}$$

where δ_1 is the pulse width and v_{ab} is in phase with current i_1. The inverter can be equivalent to a negative resistance and satisfy $-R_{ab} = 4\pi V_d \sin(\delta_1/2)/|i_1|$. It is noted that the operating frequency of the system will be determined by the transfer distance and the load, which is analyzed in detail below. According to (9), (10), and Kirchhoff's voltage and current laws, the dynamic equation of the proposed system in Fig. 2 can be expressed as

$$\begin{cases} R_{ab} i_1 = v_1 + L_1 \frac{di_1}{dt} + M \frac{di_2}{dt} + R_1 i_1 \\ 0 = v_2 + L_2 \frac{di_2}{dt} + M \frac{di_1}{dt} + (R_2 + R_v) i_2 \\ i_n = C_n \frac{dv_n}{dt}, n = 1, 2 \end{cases}. \tag{12}$$

Since the proposed FOWPT system has multiple controllable parameters, the coupled mode theory is adopted to simplify the analysis. Compared to the circuit model, the coupled model reduces the order of the differential equation by half [23], which greatly reduces the complexity of modeling and analysis. Considering that the proposed system has high-quality factor, the coupled model has a certain accuracy. More importantly, the reduction in the order of the mathematical model makes it possible to solve the characteristic frequency of the proposed system. According to the coupled mode theory [24], the relationship between state variables and forward/reverse rotation modes can be defined as

$$a_{n\pm} = \sqrt{\frac{C_n}{2}} v_n \pm j \sqrt{\frac{L_n}{2}} i_n (n = 1, 2). \tag{13}$$

Substituting (13) into (12), it can be obtained that

$$\begin{cases} \frac{d\xi_1}{dt} = -j\omega_1 \chi_1 + k \frac{d\xi_2}{dt} - 2\Gamma_1 \xi_1 + 2\sqrt{2}\xi_1 G_1 \Big/ \\ \qquad \sqrt{|a_{1+}|^2 + |a_{1-}|^2} \\ \frac{d\xi_2}{dt} = -j\omega_2 \chi_2 + k \frac{d\xi_1}{dt} - 2(\Gamma_2 + \Gamma_v) \xi_2 \\ \frac{d\chi_n}{dt} = -j\omega_n \xi_n, n = 1, 2 \end{cases} \tag{14}$$

where $\xi_n = a_{n+} - a_{n-}$ and $\chi_n = a_{n+} + a_{n-}$; $G_1 = 2V_d \sin(\delta_1/2)/\pi\sqrt{2L_1}$ is the gain coefficient; the coupling strength of M is defined as $k = M/(L_1 L_2)^{1/2}$; $\Gamma_n = R_n/2L_n$ is the intrinsic loss rate ($n = 1, 2$); $\Gamma_v = R_v/2L_2$ is the loss rate due to the load; $\omega_n = 1/\sqrt{L_n C_n}$ is the natural resonant angular frequency. Since the amplitude of the forward and reverse rotation modes are the same, the reverse rotation mode is selected for analysis. Considering high-quality factor and ignoring the second-order small quantities, the coupled mode equation (14) can be further derived as

$$\begin{cases} \frac{da_1}{dt} = \left(j\omega_1 + \frac{G_1}{|a_1|} - \Gamma_1\right) a_1 + j\kappa a_2 \\ \frac{da_2}{dt} = [j\omega_2 - (\Gamma_2 + \Gamma_v)] a_2 + j\kappa a_1 \end{cases} \tag{15}$$

where $\kappa = \sqrt{\omega_1 \omega_2} k/2$ is coupling rates between the coupled modes. Assuming the form of the solution is $a_{1,2} = \tilde{A}_{1,2} e^{i\omega t}$, the characteristic equation of (15) can be derived as

$$\left(j(\omega_1 - \omega) + \frac{G_1}{|a_1|} - \Gamma_1\right)(j(\omega_2 - \omega) - \Gamma_2 - \Gamma_v) + \kappa^2 = 0. \tag{16}$$

By separating the real and imaginary parts and variable substitution $\omega = x + 2\omega_2/3 + \omega_1/3$, (16) can be organized into a cubic equation $x^3 + px + q = 0$, where $p = -\gamma^2/3 + (\Gamma_2 + \Gamma_v)^2 - \kappa^2$, $q = 2\gamma^3/27 - \gamma[(\Gamma_2 + \Gamma_v)^2 - \kappa^2]/3 + \gamma(\Gamma_2 + \Gamma_v)^2$ and $\gamma = \omega_2 - \omega_1$. This equation can be solved by the Cardano Formula, and three characteristic frequencies can be obtained as

$$\begin{cases} \omega_{c1} = \sigma_1 + \sigma_2 + 2\omega_2/3 + \omega_1/3 \\ \omega_{c2} = \beta\sigma_1 + \beta^2\sigma_2 + 2\omega_2/3 + \omega_1/3 \\ \omega_{c3} = \beta^2\sigma_1 + \beta\sigma_2 + 2\omega_2/3 + \omega_1/3 \end{cases} \tag{17}$$

where $\beta = (-1 + \sqrt{3}i)/2$, $\Delta = (q/2)^2 + (p/3)^3$ $\sigma_1 = \sqrt[3]{-q/2 + \sqrt{\Delta}}$ and $\sigma_2 = \sqrt[3]{-q/2 - \sqrt{\Delta}}$. Δ is defined as the discriminant of the cubic equation. When $\Delta > 0$, the proposed system has a real solution and a pair of conjugate complex solutions; when $\Delta \le 0$, the proposed system has three real solutions.

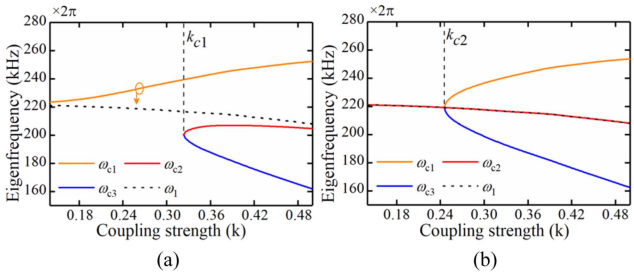

Fig. 7. Eigenfrequency as a function of coupling strength k when $R_v = 20\,\Omega$. (a) Frequency detuning $\omega_1 \neq \omega_2$. (b) Frequency matching $\omega_1 = \omega_2$.

A special case will be considered. When the system frequency matches ($\omega_1 = \omega_2$), the discriminant can be further simplified as $\Delta = \{[(\Gamma_2+\Gamma_v)^2 - \kappa^2]/3\}^3$. This system satisfies the parity-time symmetry condition [25], and the system is also divided into two areas: when $k < k_{c2}$ ($\Delta > 0$), there is one real frequency solution ω_{c1}; when $k \geq k_{c2}$ ($\Delta \leq 0$), the system has three real frequency solutions, where two stable solutions can be expressed as [26]

$$\omega_{c2,c3} = \omega_0 \pm \sqrt{\kappa^2 - (\Gamma_2 + \Gamma_v)^2} \tag{18}$$

where the corresponding critical coupling strength $k_{c2} = (R_2 + R_v)/2L_2$.

Fig. 7 depicts the characteristic frequency as a function of coupling strength k under conditions of frequency detuning and frequency matching. As shown in Fig. 7(a), when the system is detuned ($\omega_1 \neq \omega_2$), the system is divided into two regions by k_{c1}: when $k < k_{c1}$, the system has a real frequency solution ω_{c1}; when $k \geq k_{c1}$, there are three real frequency solutions. It is worth noting that in this region, ω_{c2} is an unstable frequency solution, and thus the system will not operate at this frequency [27]. The black dotted line in Fig. 7 shows the natural resonant frequency of the transmitter ω_1. Since the self-inductance of coils with ferrite varies with misalignment, the natural resonant frequency is inevitably detuned. A similar result can be obtained from Fig. 7(b) as well. However, due to changes in ω_2 and ω_1, the output characteristics do not have the robustness shown in parity-time symmetric systems.

In addition, when the detuning system is in the region of $k < k_{c2}$, the operating frequency can be adjusted by adjusting the natural resonance frequency ω_2 of the receiver. When the operating frequency ω is equal to ω_1, the system is frequency matching ($\omega_2 - \omega_1 = 0$). k_{c2} can be reasonably set by adjusting R_v. Obviously, the frequency characteristics shown in Fig. 7 provide an effective solution for the frequency tuning of the FOWPT system, which will be analyzed in detail in Section III.

Compared to circuit theory, the coupled model not only reduces the order of equations, but also obtains the characteristic frequencies of multivariable systems. Besides, according to (15) and (16), the output power and transfer efficiency of the system can be obtained as

$$P_o = \frac{2\Gamma_v \kappa^2}{(\omega - \omega_2)^2 + (\Gamma_2 + \Gamma_v)^2} \times \left[\frac{(\omega - \omega_2) G_1}{(\omega - \omega_1)(\Gamma_2 + \Gamma_v) + (\omega - \omega_2)\Gamma_1}\right]^2 \tag{19}$$

$$\eta = \frac{2\kappa^2 \Gamma_v}{2\left[(\omega - \omega_2)^2 + (\Gamma_2 + \Gamma_v)^2\right]\Gamma_1 + 2\kappa^2(\Gamma_2 + \Gamma_v)}. \tag{20}$$

III. System Design and Control Strategy

Under the actual operating conditions, fluctuations in transfer distance, load, and inductance have significant effects on the robustness of the WPT system. In order to overcome these problems, this section will provide a detailed analysis of system design, frequency tuning strategies, and CC/CV control strategies.

A. System Design

In the proposed system, the transmitter and receiver are integer-order circuits and fractional-order circuits, respectively. According to operation modes of the fractance element in Fig. 3, reducing the adjustment range of δ_2 is conducive to achieving soft switching and increasing the adjustment ability of detuning. Therefore, the frequency and duty of the transmitter are designed to have CC or CV output characteristics, while the fractance element of the receiver provides frequency tuning and high-accuracy output. The misalignment tolerance and detuning tolerance can be achieved by the coordination of integer-order circuits and fractional-order circuits.

Under the ideal conditions of $\omega_1 = \omega_2 = \omega_0 = 2\pi f_0$ and ignoring the internal resistance of circuits ($R_1 = R_2 = 0$), when the output voltage v_{ab} of the inverter is in phase with i_{2s}, the system will maintain CV output independent of the load [28]. The corresponding operating frequency is $f_H = f_0/\sqrt{1-k}$ or $f_L = f_0/\sqrt{1+k}$. In this case, the voltage gain G_v of the output voltage v_o to the voltage v_{ab} of the inverter can be derived as

$$G_v = \sqrt{\frac{L_2}{L_1}}. \tag{21}$$

It can be found that the voltage gain is only related to self-inductance when the system operates at frequency f_H or f_L. Obviously, when self-inductance varies with misalignment, the voltage gain G_v will also change. Considering the adjustment range of the equivalent resistance R_v of the fractance element, this voltage gain G_v should be set to the maximum value $\sqrt{L_{2\max}/L_{1\min}}$ to satisfy the requirements of output power in the entire charging region.

It should be noted that the load-independent CV output characteristics need strict constraints. On the one hand, it is required that the resonant frequencies $\omega_1 = \omega_2 = \omega_0 = 2\pi f_0$ and the internal resistance $R_1 = R_2 = 0$. On the other hand, it is required that the ratio of the self-inductance is constant. In application, these conditions are difficult to satisfy because of misalignment, which seriously affect the CV characteristics. Therefore, the designed system should have the ability of frequency tuning and rely on the fractance element to correct the output.

When the condition of $\omega_1 = \omega_2 = \omega_0 = 2\pi f_0$ can be satisfied and the operating frequency is also set to f_0, the system has a CC output characteristic. In this case, the current gain G_i of the output current i_o to the voltage v_{ab} of the inverter can be derived

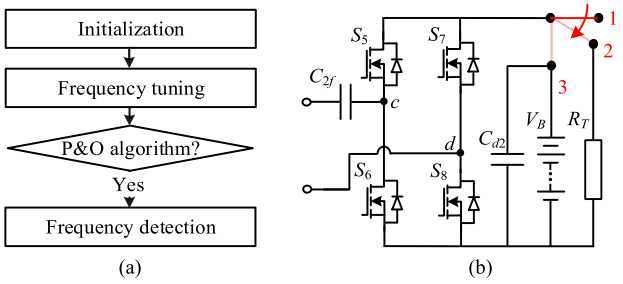

Fig. 8. (a) Flow chart of frequency tuning. (b) Switching circuit of the receiver.

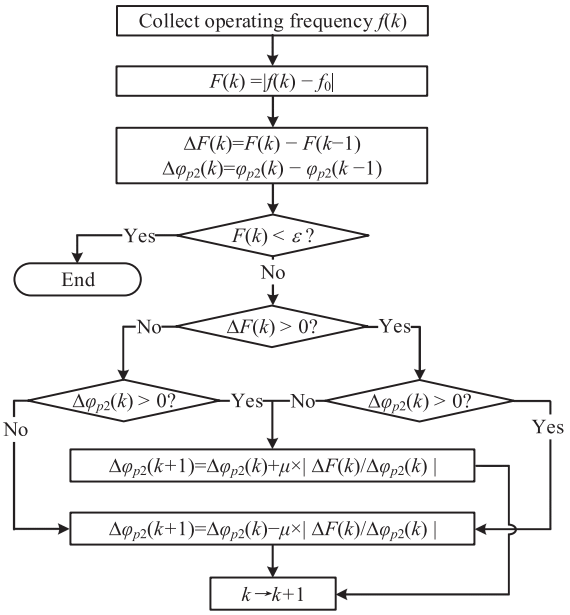

Fig. 9. Improved P&O algorithm.

as $1/2\pi f_0 M$. According to the definitions of resonance frequency f_0 and f_H, the gain coefficient G_i can be derived as

$$G_i = \frac{f_H^2\sqrt{C_1}}{(f_H^2 - f_0^2)\sqrt{L_2}} \tag{22}$$

where self-inductance L_2 is taken as the minimum value $L_{2\min}$ over the charging region, and thus the gain coefficient can meet the output power requirements over the entire charging range.

B. Frequency Tuning

Fig. 8 shows the flow chart and switching circuit of the receiver. The entire charging process can be divided into the following three stages.

1) Initialization: The transmitter is controlled in zero-phase mode (v_{ab} and i_1 are in phase) with a small initial pulse width. When the receiver with no load enters the charging region, the transmitter records the no-load frequency f_0 and operates at this frequency.
2) Frequency tuning: After the switch in Fig. 8(b) is switched from 1 to 2, the transmitter operates in zero-phase mode. Start the improved P&O algorithm in Fig. 9 to adjust the fractional order of the fractance element. Meanwhile, the operating frequency range and initial frequency of the transmitter are limited to the high-frequency band. After the P&O algorithm ends, record the corresponding $C_{2\mathrm{ref}}$.
3) Frequency detection: The equivalent resistance R_v and capacitance C_2 of the fractance element are controlled to R_S and $C_{2\mathrm{ref}}$, and record the corresponding frequency f_T. Finally, the switch is switched from 2 to 3 to start wireless charging.

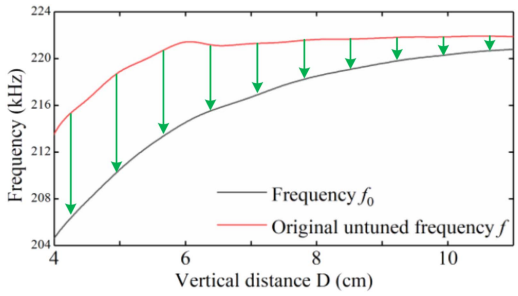

Fig. 10. Adjustment process of operating frequency when $R_T = 80\ \Omega$.

Fig. 9 shows the improved P&O algorithm for frequency tuning based on the fractance element. The improved P&O algorithm is a variable step-size algorithm, where the constant μ is a scale factor. In order to ensure the convergence of the algorithm, the scale factor μ needs to meet the constraints shown in (23), where $\Delta\varphi_{p2\max}$ is the maximum disturbance step size allowed by the fixed step size algorithm. Besides, to prevent the impact of large disturbance step sizes on system stability, it is necessary to limit the adjustment range of φ_{p2}

$$\mu \le \Delta\varphi_{p2\max} \Big/ \left|\frac{\Delta F}{\Delta\varphi_{p2}}\right|. \tag{23}$$

Fig. 10 shows the adjustment process of operating frequency. Benefiting from the fractance element with adjustable order and the P&O algorithm, the operating frequency gradually approaches the black curve from the red curve. When the operating frequency approaches the no-load frequency f_0 at the current position, the natural resonant frequencies of the transmitter and receiver remain consistent ($\omega_1 = \omega_2 = \omega_0 = 2\pi f_0$), and the tuning process is completed. The effectiveness of the tuning process will be demonstrated in the experimental section.

According to the frequency tuning strategy and the frequency characteristic of the zero-phase mode, the frequency f_H of the transmitter in CV mode can also be obtained. Considering the expression $f_H = f_0/\sqrt{1-k}$ and (18), f_H can be derived as

$$f_H = \frac{f_0}{\sqrt{1 - \frac{2}{f_0}\sqrt{(f_T - f_0)^2 + \left(\frac{\Gamma_2+\Gamma_S}{2\pi}\right)^2}}} \tag{24}$$

where $\Gamma_S = R_S/2L_2$; f_T is obtained from Fig. 8(a); the equivalent resistance R_S is set to 10 Ω and its corresponding critical coupling strength k_{c2} is 0.12. Different from the closed-loop control, when the equivalent resistance R_v and capacitance C_2 are set separately, the coupling relationship between pulse width δ_2 and phase φ_{p2} needs to be considered. Therefore, according

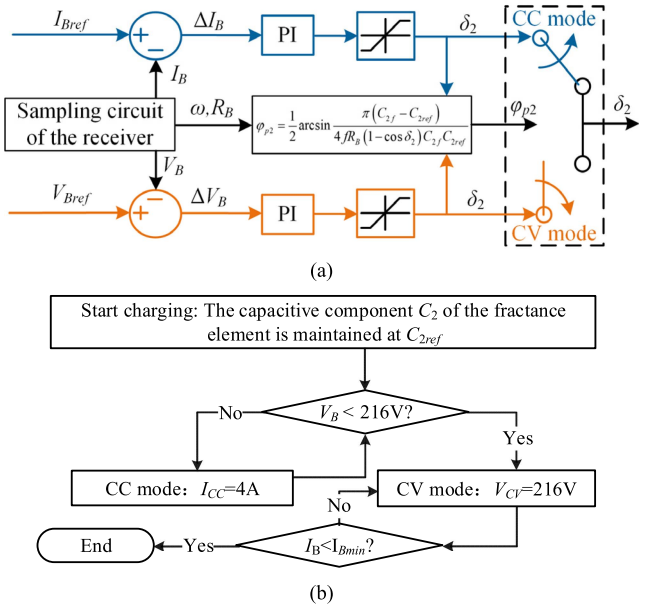

Fig. 11. (a) Control block diagram and (b) flow chart of CC and CV mode in the receiver.

to (9) and (10), δ_2 and φ_{p2} can be decoupled as

$$\begin{cases} \varphi_{p2} = \arctan\frac{C_{2f}-C_{2\text{ref}}}{2\pi f C_{2\text{ref}} C_{2f} R_S} \\ \delta_2 = \arccos\left(1-\frac{\pi^2 R_S}{4R_T\cos^2\varphi_{p2}}\right) \end{cases}. \tag{25}$$

C. Design of the Control Strategy

After frequency tuning and obtaining the corresponding $C_{2\text{ref}}$ at the current position, the fractance element needs to maintain the frequency matching ($\gamma = \omega_2 - \omega_1 = 0$) during the charging process, that is, the capacitance component $C_{2\text{ref}}$ should be maintained constant. According to the designed tuning process in Fig. 9 and (10), the phase φ_{p2} can be deduced as

$$\varphi_{p2} = \frac{1}{2}\arcsin\frac{\pi\left(C_{2f}-C_{2\text{ref}}\right)}{4fR_B\left(1-\cos\delta_2\right)C_{2f}C_{2\text{ref}}} \tag{26}$$

where the operating frequency f is set to f_0 and f_H in the CC mode and CV mode, respectively. The operating frequency is controlled by the transmitter. For the receiver, Fig. 11(a) gives the control block diagrams of CC and CV modes. The proposed system can achieve CC or CV output by jointly adjusting the pulse width δ_2 and phase φ_{p2} of the fractance element. Fig. 11(b) gives the flow chart of the receiver. When starting wireless charging, the fractance element operates in CC mode or CV mode according to the information of battery and maintains the equivalent capacitance C_2 equal to $C_{2\text{ref}}$ by adjusting the fractional order. When the receiver is in CV mode and the output current is less than the cutoff current $I_{B\min} = 0.4$ A, the charging process ends.

In order to ensure that the system can provide sufficient output power to maintain CC or CV over the entire charging range, it is necessary to design the dc voltage source V_d of the transmitter. Considering that the fractance element can reduce the equivalent

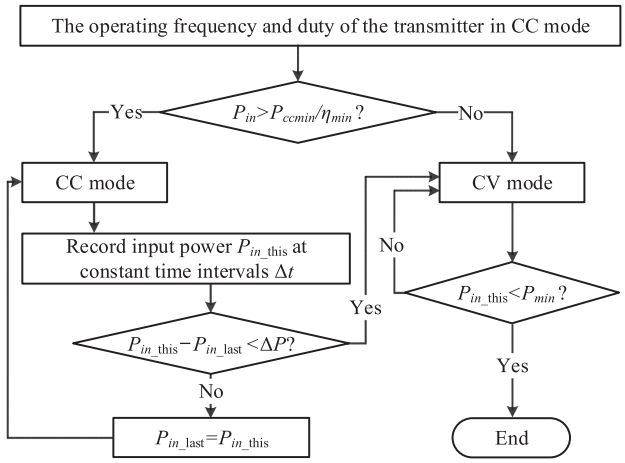

Fig. 12. Flow chart of transmitter during the charging process.

resistance of the load within a certain range, the output characteristics should have an output margin to make it possible for the fractance element to adjust the output power. This characteristic is mainly determined by the operating frequency and duty of the transmitter. Fig. 12 gives the flow chart of the transmitter. First, the transmitter operates in CC mode. When the dc input power P_{in} is greater than the minimum input power $P_{\text{ccmin}}/\eta_{\min}$ in CC mode, the transmitter continues to operate in CC mode, and the corresponding operating frequency and duty are f_0 and D_{c1_cc}, respectively. When $P_{\text{in}} \le P_{\text{ccmin}}/\eta_{\min}$, the transmitter turns on CV mode, and the corresponding operating frequency and duty are f_H and D_{c1_cv}, respectively. Therefore, the curve of output power under initial conditions can be depicted as the purple curve in Fig. 13(a). The black curve depicts the power required by the battery, where R_v of the battery is derived according to (9) and (26). In order to achieve CC output required by the load, according to (2), (6), and (22), the duty D_{c1_cc} can be derived as

$$D_{c1\_\text{cc}} = \frac{2}{\pi}\arcsin\frac{K_{\text{cc}}\pi^2 I_{\text{ref}}}{8G_i V_d} \tag{27}$$

where K_{cc} is the margin coefficient of current, taken as greater than 1. Similarly, according to (2) and (21), it can be deduced that the duty in CC mode is

$$D_{c1\_\text{cv}} = \frac{2}{\pi}\arcsin\frac{K_{\text{cv}} V_{\text{ref}}}{V_d G_v} \tag{28}$$

where K_{cv} is the margin coefficient of voltage, taken as less than 1. The margin coefficients are beneficial for improving the robustness of the system under parameter fluctuations and also take into account the errors of frequency tuning and model. The deviation of the output is finally adjusted by the fractance element according to Fig. 11(a).

The green track and the red track in Fig. 13(b) show the charging process under different battery states. According to the flow chart in Figs. 8(a) and 11, the fractance element of the receiver participate in frequency tuning and output control. When the system switches from CC mode to CV mode, the receiver switches the closed-loop control strategy first. After detecting a decrease in power, the transmitter switches to the operating frequency and duty of CV mode. When the power is

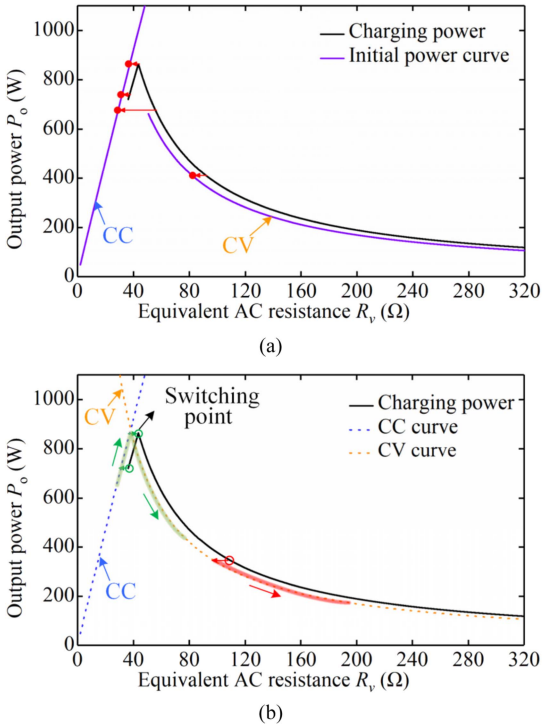

Fig. 13. Charging curve of the load and output power characteristic of the system. (a) Output power characteristic curve under initial conditions. (b) Charging process under different battery states.

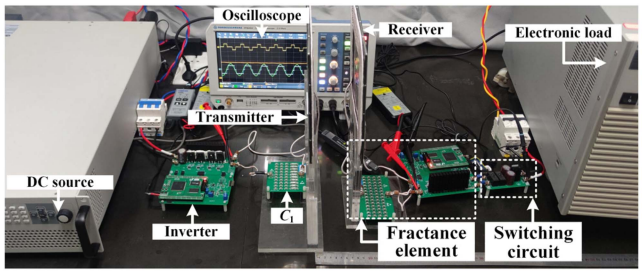

Fig. 14. Experimental prototype of the proposed system.

less than the set value $P_{\min}$, wireless charging will be stopped. It can be seen that the proposed control strategy of the transmitter greatly improves the adjustable load range and is also conducive to the realization of soft switching. Through the coordination of integer-order circuits in the transmitter and fractional-order circuits in the receiver, a CC/CV wireless charging with misalignment tolerance and detuning tolerance can be achieved.

IV. Experiment

A. Design of the Prototype

This section will validate the feasibility of the proposed method by constructing a FOWPT system. Besides, misalignment tolerance, detuning tolerance, and output accuracy of this system will also be verified. The experimental prototype is shown in Fig. 14. In the power circuit, MOSFETs are IMW120R030M1H; in the control circuit, the transmitting and receiving controllers are DSP TMS320F28377D; the coil adopts

TABLE I
Configuration of the Proposed System

Symbol	Description	Value
V_d	DC input voltage	320 V
R_1	Internal resistance of transmitter	260 mΩ
R_2	Internal resistance of receiver	140 mΩ
R_T	Resistance of frequency tuning	80 Ω
C_1	Capacitor of transmitter	4 nF
C_{2f}	Capacitor of fractance element	9.33 nF
L_1	Self-inductance of Tx coil	130.5–142 μH
L_2	Self-inductance of Rx coil	59–63.2 μH
$\omega_{1,2}/2\pi$	Natural resonance frequency	208–220 kHz
D	Vertical transfer distance	5–10 cm
ρ	Offset transfer distance	0–8 cm
R_B	Equivalent resistance of battery	45–54 (CC) 54–540 (CV)

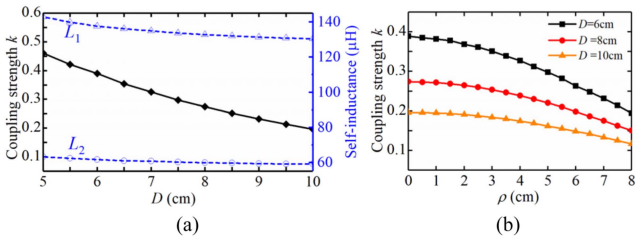

Fig. 15. Coupling strength k and self-inductance $L_{1,2}$ as a function of vertical distance D and offset distance ρ.

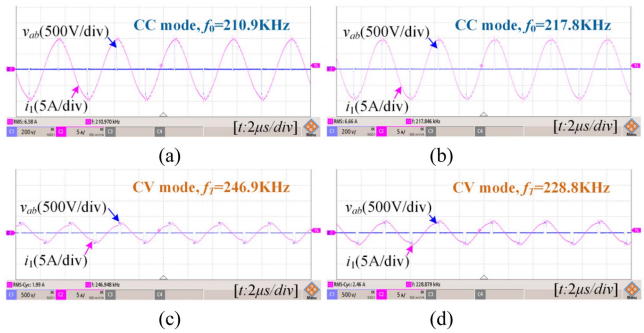

Fig. 16. Frequency detection in zero-phase mode. (a) $D = 5$ cm, $\rho = 0$ cm. (b) $D = 8$ cm, $\rho = 0$ cm. (c) $D = 8$ cm, $\rho = 0$ cm. (d) $D = 8$ cm, $\rho = 8$ cm.

Φ0.05 mm × 2000 silk-covered wire. In addition, the parameter configurations of the proposed system are given in Table I.

To verify the tolerance for misalignment and frequency detuning, Fig. 15 gives the coupling strength k and self-inductance $L_{1,2}$ as a function of vertical distance D and offset distance ρ.

B. Experiment Result

First, according to the strategy shown in Fig. 8, the frequencies f_0 and f_T can be detected before charging when the transmitter is in zero-phase mode. Fig. 16 shows the frequencies f_0 and f_T in the no-load condition and the tuned state, respectively. Then, according to (24), (27), and (28), the operating frequency and duty of the transmitter in CC and CV modes can be derived.

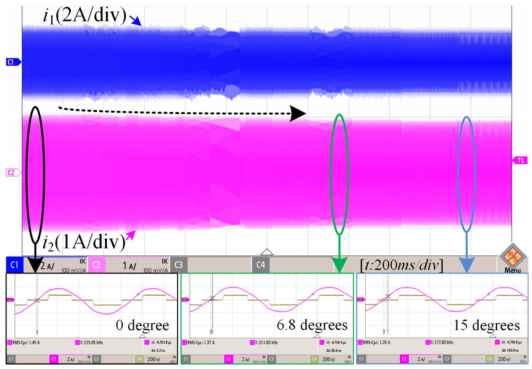

Fig. 17. Frequency tuning process when $D = 8$ cm, $\rho = 0$ cm.

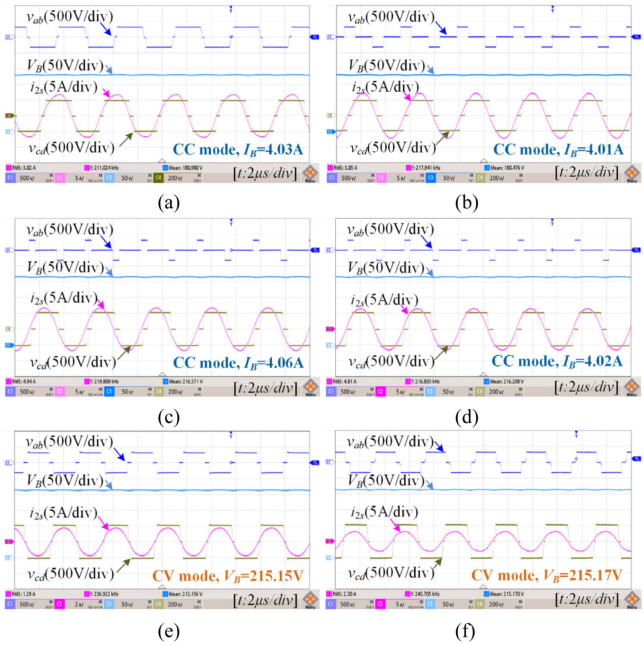

Fig. 18. Experimental waveforms. (a) $D = 5$ cm, $\rho = 0$ cm, R_B=45 Ω. (b) $D = 8$ cm, $\rho = 0$ cm, $R_B = 45$ Ω. (c) $D = 10$ cm, $\rho = 0$ cm, $R_B = 54$ Ω. (d) $D = 8$ cm, $\rho = 8$ cm, $R_B = 54$ Ω. (e) $D = 8$ cm, $\rho = 8$ cm, $R_B = 200$ Ω. (f) $D = 10$ cm, $\rho = 0$ cm, $R_B = 120$ Ω.

Fig. 17 gives the frequency tuning process. To demonstrate the frequency tuning strategy of the FOWPT system, a 5 μH inductor is connected in series on the receiving side to increase the detuning. In this case, frequency tuning can still be achieved by adjusting the order of the fractance element. The phase angle of i_{2s} and v_{cd} gradually changes from 0 to 15 degrees, so that the operating frequency satisfies $|f(k) - f_0| < \varepsilon$ and the corresponding $C_{2\text{ref}} = 8.27$ nF. The tuning strategy has been verified, which improves the efficiency and provides conditions for the CC/CV control strategy.

Fig. 18 is the steady-state waveform of the system, which shows the misalignment tolerance and CC/CV output accuracy of the tuned system. With the precise adjustment of the fractance element on the receiving side, the system can ensure CC and CV outputs. Benefiting from operation modes of the fractance element in Section II and the control strategy of CC/CV modes in Section III, the proposed system can achieve soft switching in

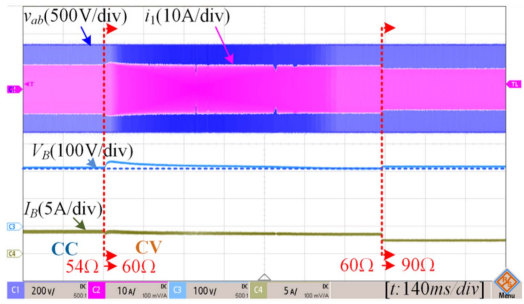

Fig. 19. Dynamic process of CC and CV mode switching.

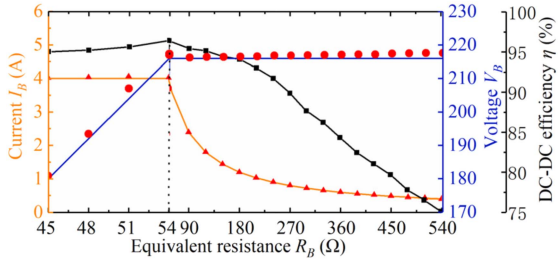

Fig. 20. Experimental results of the current I_B and voltage V_B and dc–dc efficiency η in the charging process.

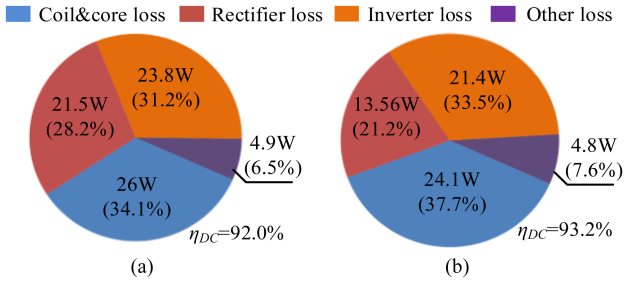

Fig. 21. Power loss under different cases. (a) Without frequency tuning. (b) With frequency tuning.

most charging regions. Besides, Fig. 19 verifies the switching of CC and CV control strategies of the transmitter in Figs. 11 and 12. When the load is switched from 54 to 60 Ω, the transmitter can smoothly switch from CC mode to CV mode. For the step change in CV mode, the fractance element can also respond quickly.

To demonstrate the output accuracy during the charging process, Fig. 20 gives the current I_B and voltage V_B and dc–dc efficiency η in the charging process when $D = 8$ cm. With the help of soft switching, the highest dc–dc efficiency η is 95.1%. The experimental results show that the proposed system has a high-accuracy CC/CV output in the case of frequency detuning and wide load range.

Due to the misalignment and parameter drift, frequency detuning is inevitable in practical applications. In this experimental prototype, the natural resonant frequency ($\omega_1/2\pi$) of the transmitter is higher than that of the receiver ($\omega_2/2\pi$). As the coupling strength k decreases, the degree of frequency detuning will gradually increase. Fig. 21 shows the power loss without and with frequency tuning when $k = 0.196$. Benefiting from the

TABLE II
COMPARISONS WITH PREVIOUS WORKS

Reference	[3]	[4]	[9]	[11]	[14]	**This work**
Rx Coil size (cm)	11×11	15×15	NA	45×45	36×36	20×20
No. of passive components	7	8	8	9	8	4
No. of Switches/diodes	4/4	6/4	6/2	4/4	8/4	8/0
Misalignment of D and ρ (cm)	D: N/A ρ: N/A	D: 2 ρ: 0	NA NA	D: 15 ρ: 0–18	D: 6–12 ρ: 0–12	D: 5–10 ρ: 0–8
Range of k	0.14–0.28	0.491	0.19	0.073–0.076	0.1–0.44	0.196–0.46
Frequency tuning	No	No	No	No	SCC	FOWPT
Soft switching	ZVS	ZVS	No	ZVS	ZPA	ZVS
CC/CV	No	CC/CV	CC/CV	CC	No	CC/CV

frequency tuning and ZVS, rectifier loss is effectively reduced and the dc–dc efficiency can be improved by 1.2%.

C. Discussion and Comparison

Table II compares the proposed system in this article to those in previous works. It is worth noting that quantitative comparisons are unfair due to differences in the parameters of different works. Therefore, qualitative comparison is of concern. Compared with the parameter design [3], this method has higher output accuracy. Compared with the passive high-order compensation topology [4], the proposed system has fewer passive components. Compared with the secondary active rectifier control scheme [9], both methods can achieve high-accuracy CC/CV without wireless communication. Benefiting from the proposed control strategy and parameter design, this method can also achieve frequency tuning and ZVS. Compared with the new coil design [11], this method does not require a complex coil design, and the offset direction is arbitrary. Compared to active matching [14], this method has no power limitations and fewer components. In this article, under wide coupling coefficient and load conditions, the transmitter provides a wide range of adjustments for power and CC/CV characteristics by controlling operating frequency and duty. Meanwhile, the fractance element achieves frequency tuning and adjustment of output based on the frequency characteristic and designed control strategy. Therefore, the proposed system has misalignment and detuning tolerance under a wide range of coupling and loads. This is valuable for the widespread application and industrial promotion of wireless charging.

V. CONCLUSION

In this article, aiming at improving the system efficiency and the accuracy of CC/CV, a FOWPT system with adjustable order is proposed. According to the operation modes of the fractance element and the coupled model of the detuned system, the tuning strategy and the CC/CV control strategy of transmitter and receiver are proposed, respectively. The proposed strategies have been verified by an 864-W prototype, which achieves soft switching and widens the load range (45–540 Ω). The proposed system has high-accuracy CC or CV output under conditions of misalignment and frequency detuning, which is crucial to the application of wireless charging. In future work, we will focus on the tuning and CC/CV control strategy in dynamic wireless charging based on fractional-order circuits.

REFERENCES

[1] Z. Zhang, H. Pang, A. Georgiadis, and C. Cecati, "Wireless power transfer—An overview," *IEEE Trans. Ind. Electron.*, vol. 66, no. 2, pp. 1044–1058, Feb. 2019.

[2] R. Yue, C. Wang, H. Li, and Y. Liu, "Constant-voltage and constant-current output using P-CLCL compensation circuit for single-switch inductive power transfer," *IEEE Trans. Power Electron.*, vol. 36, no. 5, pp. 5181–5190, May 2021.

[3] H. Feng, A. Dayerizadeh, and S. M. Lukic, "A coupling-insensitive X-type IPT system for high position tolerance," *IEEE Trans. Ind. Electron.*, vol. 68, no. 8, pp. 6917–6926, Aug. 2021.

[4] Y. Li et al., "Reconfigurable intermediate resonant circuit based WPT system with load-independent constant output current and voltage for charging battery," *IEEE Trans. Power Electron.*, vol. 34, no. 3, pp. 1988–1992, Mar. 2019.

[5] K. Song, Z. Li, J. Jiang, and C. Zhu, "Constant current/voltage charging operation for series–Series and series–Parallel compensated wireless power transfer systems employing primary-side controller," *IEEE Trans. Power Electron.*, vol. 33, no. 9, pp. 8065–8080, Sep. 2018.

[6] J. Luo et al., "Novel cuk-based bridgeless rectifier of wireless power transfer system with wide power modulation range and low current ripple," *IEEE Trans. Ind. Electron.*, vol. 69, no. 3, pp. 2533–2544, Mar. 2022.

[7] Y. Chen, S. He, B. Yang, S. Chen, Z. He, and R. Mai, "Reconfigurable rectifier-based detuned series-series compensated IPT system for anti-misalignment and efficiency improvement," *IEEE Trans. Power Electron.*, vol. 38, no. 2, pp. 2720–2729, Feb. 2023.

[8] Y. Chen et al., "A clamp circuit-based inductive power transfer system with reconfigurable rectifier tolerating extensive coupling variations," *IEEE Trans. Power Electron.*, to be published, 2023.

[9] S. Zou, O. C. Onar, V. Galigekere, J. Pries, G.-J. Su, and A. Khaligh, "Secondary active rectifier control scheme for a wireless power transfer system with double-sided LCC compensation topology," in *Proc. IEEE 44th Annu. Conf. Ind. Electron. Soc.*, 2018, pp. 2145–2150.

[10] K. Song et al., "Design of DD coil with high misalignment tolerance and low EMF emissions for wireless electric vehicle charging systems," *IEEE Trans. Power Electron.*, vol. 35, no. 9, pp. 9034–9045, Sep. 2020.

[11] Y. Chen, R. Mai, Y. Zhang, M. Li, and Z. He, "Improving misalignment tolerance for IPT system using a third-coil," *IEEE Trans. Power Electron.*, vol. 34, no. 4, pp. 3009–3013, Apr. 2019.

[12] J. Mai, Y. Wang, Y. Yao, M. Sun, and D. Xu, "High-misalignment-tolerant IPT systems with solenoid and double D pads," *IEEE Trans. Ind. Electron.*, vol. 69, no. 4, pp. 3527–3535, Apr. 2022.

[13] H. Kennedy, R. Bodnar, T. Lee, and W. Redman-White, "A self-tuning resonant-inductive-link transmit driver using quadrature symmetric delay trimmable phase-switched fractional capacitance," *IEEE J. Solid-St. Circ.*, vol. 53, no. 6, pp. 1694–1706, Jun. 2018.

[14] P. Tan, B. Song, W. Lei, H. Yin, and B. Zhang, "Decoupling control of double-side frequency tuning for LCC/S WPT system," *IEEE Trans. Ind. Electron.*, vol. 70, no. 11, pp. 11163–11173, Nov. 2023.

[15] E. S. Lee, B. G. Choi, J. S. Choi, D. T. Nguyen, and C. T. Rim, "Wide-range adaptive IPT using dipole-coils with a reflector by variable switched capacitance," *IEEE Trans. Power Electron.*, vol. 32, no. 10, pp. 8054–8070, Oct. 2017.

[16] W. Li, Q. Zhang, C. Cui, and G. Wei, "A self-tuning S/S compensation WPT system without parameter recognition," *IEEE Trans. Ind. Electron.*, vol. 69, no. 7, pp. 6741–6750, Jul. 2022.
[17] X. Zhu et al., "High-efficiency WPT system for CC/CV charging based on double-half-bridge inverter topology with variable inductors," *IEEE Trans. Power Electron.*, vol. 37, no. 2, pp. 2437–2448, Feb. 2022.
[18] Y. Li et al., "Extension of ZVS region of series–Series WPT systems by an auxiliary variable inductor for improving efficiency," *IEEE Trans. Power Electron.*, vol. 36, no. 7, pp. 7513–7525, Jul. 2021.
[19] B. T. Krishna, "Recent developments on the realization of fractance device," *Fract. Calc. Appl. Anal.*, vol. 24, no. 6, pp. 1831–1852, Oct. 2021.
[20] D. Guo, D. Li, H. Yin, H. Lan, and C. Kong, "Simplified analysis and characterization of dual power source wireless power transfer system," *IEEE J. Emerg. Sel. Topics Ind. Electron.*, vol. 4, no. 3, pp. 948–959, Jul. 2023, doi: 10.1109/JESTIE.2023.3276711.
[21] C. Rong, B. Zhang, Y. Jiang, X. Shu, and Z. Wei, "A misalignment-tolerant fractional-order wireless charging system with constant current or voltage output," *IEEE Trans. Power Electron.*, vol. 37, no. 9, pp. 11356–11368, Sep. 2022.
[22] K. Biswas et al., *Fractional-order Devices*. Cham, Switzerland: Springer International Publishing, 2017.
[23] M. Kiani and M. Ghovanloo, "The circuit theory behind coupled-mode magnetic resonance-based wireless power transmission," *IEEE Trans. Circuits Syst. I, Reg. Papers*, vol. 59, no. 9, pp. 2065–2074, Sep. 2012.
[24] H. Li, K. Wang, L. Huang, W. Chen, and X. Yang, "Dynamic modeling based on coupled modes for wireless power transfer systems," *IEEE Trans. Power Electron.*, vol. 30, no. 11, pp. 6245–6253, Nov. 2015.
[25] S. Assawaworrarit, X. Yu, and S. Fan, "Robust wireless power transfer using a nonlinear parity-time-symmetric circuit," *Nature*, vol. 546, no. 7658, pp. 387–390, Jun. 2017.
[26] C. Rong, B. Zhang, Z. Wei, L. Wu, and X. Shu, "A wireless power transfer system for spinal cord stimulation based on generalized parity–Time symmetry condition," *IEEE Trans. Ind. Appl.*, vol. 58, no. 1, pp. 1330–1339, Jan./Feb. 2022.
[27] A. U. Hassan, H. Hodaei, M. A. Miri, M. Khajavikhan, and D. N. Christodoulides, "Nonlinear reversal of the PT-symmetric phase transition in a system of coupled semiconductor micro-ring resonators," *Phys. Rev. A*, vol. 92, no. 6, Dec. 2015, Art. no. 063807.
[28] E. Gati, G. Kampitsis, and S. Manias, "Variable frequency controller for inductive power transfer in dynamic conditions," *IEEE Trans. Power Electron.*, vol. 32, no. 2, pp. 1684–1696, Feb. 2017.

Chao Rong was born in Shanxi, China, in 1995. He received the B.S. degree in electrical engineering and automation in 2018 from the South China University of Technology, Guangzhou, China, where he is currently working toward the Ph.D. degree in power electronics and power drives.

His current research interests include wireless power transfer technology and fractional-order system.

Bo Zhang (Senior Member, IEEE) was born in Shanghai, China, in 1962. He received the B.S. degree in electrical engineering from the Zhejiang University, Hangzhou, China, in 1982, the M.S. degree in power electronics from the Southwest Jiaotong University, Chengdu, China, in 1988, and the Ph.D. degree in power electronics from the Nanjing University of Aeronautics and Astronautics, Nanjing, China, in 1994.

He is currently a Professor with the School of Electric Power, South China University of Technology, Guangzhou, China. He has authored or co-authored over 600 papers and held over 170 patents. He has authored nine monographs. His research interests include nonlinear analysis and control of power electronics, wireless power transfer technology, and ac drives.